# Analysis of gasification biochar from lignocellulosic waste for high performance biographite anode

Weijers, Mark; Mulder, Fokko M.; Cutz, Luis

**DOI**
10.1016/j.biombioe.2025.108147

**Publication date**
2025

**Document Version**
Final published version

**Published in**
Biomass and Bioenergy

**Citation (APA)**
Weijers, M., Mulder, F. M., & Cutz, L. (2025). Analysis of gasification biochar from lignocellulosic waste for high performance biographite anode. *Biomass and Bioenergy*, *201*, Article 108147. https://doi.org/10.1016/j.biombioe.2025.108147

Biomass and Bioenergy 201 (2025) 108147

Contents lists available at ScienceDirect

Biomass and Bioenergy

journal homepage: www.elsevier.com/locate/biombioe

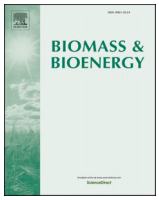

# Analysis of gasification biochar from lignocellulosic waste for high performance biographite anode

Mark Weijers [a], Fokko M. Mulder [a], Luis Cutz [b,*]

[a] Faculty of Applied Sciences, Chemical Engineering Department, Delft University of Technology, Van der Maasweg 9, Delft, 2629HZ the Netherlands
[b] Process and Energy Department, University of Technology of Delft, Leeghwaterstraat 39, 2628 CB Delft, the Netherlands

ARTICLE INFO

*Keywords:*
Lithium-ion battery
Graphite
Anode
Gasification
Biochar
Biomass
Biographite

ABSTRACT

Renewable graphite from low-grade waste is an alternative for fossil-derived graphite for anodes in lithium-ion batteries. This study investigates into whether the biochar produced from indirect biomass gasification can be used as lithium anode active material after graphitization. In this study, we focus on the biochar by-product from gasified wood pellets using a novel 50 kWth Indirectly Heated Bubbling Fluidized Bed Steam Reformer (IHBFBSR) design. The resulting biographite is analyzed according to its crystallinity, morphology, surface composition and subsurface composition. Also, the material is tested in half cell batteries to determine its suitability for lithium-ion batteries. The biographite shows a high crystallinity which is necessary for good lithium diffusivity in the lattice structure. However, the biographite flakes are not homogeneous in size. Testing in half cell batteries demonstrated that 96 % of the theoretical graphite capacity is reached. The material shows capacity fade linked to exfoliation of the material. The initial coulombic efficiency (ICE) during charging is lower than conventional graphites due to surface reactivity. Size distribution, exfoliation and ICE must therefore be addressed to make the IHBFBSR biographite fit for battery utility.

## 1. Introduction

Nowadays, renewable sourcing of materials is becoming increasingly important in view of concerns regarding the availability and sustainability [1] of conventional resources which are required for large scale electric vehicle (EV) manufacturing. Up to now, conventional resources for lithium battery anode grade graphites include non-renewable mineral graphite and synthetic graphite, which are either mined or produced from petroleum coke at extreme temperatures (≅ 3000 °C) respectively [2]. Furthermore, the uneven global distribution of graphite means that some countries may face supply chain disruptions, which could impact the manufacturing of EVs that depend on these materials. Therefore graphite is identified as 'strategic material' by the European Commission [3].

In the battery industry, mineral or synthetic graphite are of high interest as anode active material in lithium-ion batteries (LIB). These graphites are highly ordered, have moderate gravimetric capacity, long cycle life and a low working potential for lithium intercalation [4–7]. Ordered graphite sheets allows a high degree of lithium intercalation with low resistance [6]. Alternative anode materials in the form of silicon/graphite [8], silicon [9] and lithium metal [10,11] are currently emerging. These alternative materials face a high standard since the stability of graphite anodes is unprecedented [12]. For applications which need long term stability rather than high volumetric capacity, graphite still remains the first choice. Another reason to use graphite anodes is their lower cost when compared to the alternatives mentioned above. In a typical battery chemistry, 7 % of the cost is associated with the raw material [13]. For example, the cost associated with silicon is sixfold compared to graphite (assuming SiO) [14]. Given graphite's cost competitiveness and performance in the lithium-ion battery field, developing a sustainable alternative, such as using biochar to produce biographite, remains a good investment in the near future.

Biochar is a product or by-product of biomass thermochemical conversion processes such as torrefaction [15], pyrolysis, gasification [16], hydrothermal carbonization (HTC) [17] and hydrothermal liquefaction (HTL) [18,19]. Biochar produced from biomass resources offers an advantage due to their low embodied carbon and renewable nature which would relief the usage of fossil-based graphite. To ensure good EV battery performance while using biochar as a precursor of anode active material, the biochar must have similar characteristics as the state-of-the art materials. Key performance indicators of such characteristics are showing negligible coulombic inefficiencies and high capacity retention

* Corresponding author.
*E-mail address:* luis.cutz@tudelft.nl (L. Cutz).

https://doi.org/10.1016/j.biombioe.2025.108147
Received 8 November 2024; Received in revised form 26 June 2025; Accepted 30 June 2025
Available online 8 July 2025

in lithium-ion batteries [20].

In biomass gasification, the majority of attention has been focused on producing and upgrading the syngas from the gasification process. The gasification biochar is still considered a byproduct in this process as it is only a few percent of the carbon balance. Hence biochar valorization from gasifiers is still limited. Up to now the majority of research has focused on the use of biochar as adsorbent materials and soil amendment [16,21]. Nevertheless, the majority of these solutions are still at lab or prototype scale. This is because the properties of biochar are highly influenced by the type of feedstock, thermochemical technology, reactor type and scale. Meanwhile, the biofuel industry is witnessing tremendous growth. Thus, focusing on the use of biochar from gasifiers is critical because companies that produce large amounts of biochar may face a risk or an opportunity, depending on whether or not they can find a profitable use for this material.

The main challenges regarding the use of biochar as a precursor for anode materials for lithium-ion batteries directly are its poor pore features, surface functionalization, and maintaining carbon conversion efficiency while not affecting biochar properties. Impurities in biochar can make downstream purification more challenging [22]. Some of these challenges could be solved by combining a thermochemical process followed by a graphitization process to produce an ordered and high-performance graphite for lithium battery anodes. Thus, recent studies evaluate the use of a thermochemical process to create the biochar, which is then graphitized to turn the amorphous carbon structure of biochar into crystalline graphitic carbon, known as biographite [4,5,23,24]. Biographite has gained attention as material for lithium-ion batteries due to its low surface area after carbon coating, reduced coulombic losses, and good packing efficiency which increases volumetric and areal capacity when used in lithium-ion batteries [5]. Biographite, which is derived typically from slow pyrolysis (400 °C–600 °C) has been successfully obtained from a variety of feedstocks (wood flour, corncobs, medium-density fiberboard derived from recycled wood biomass, softwood, among others), providing good performance in terms of reversible capacity (307 mAh/g − 353 mAh/g) [4,5,23].

According to one study [25], gasification, torrefaction, and HTC are rarely chosen since they do not frequently match the definition of biochar as defined in the European Biochar Certificate standards (EBC) [26]. Nonetheless, it is known that biochars coming from gasification are known to have higher stability, high specific surface area (SSA), lower content of poly-aromatic hydrocarbons (PAH) and are more porous than alternative technologies such as pyrolysis [27]. This is mainly attributed to the gasification temperature (600 °C–750 °C) which is relatively higher than slow pyrolysis (400 °C–600 °C) [16,27]. Still biochar from gasification has not yet been extensively investigated for potential useful uses, such as anodes for lithium-ion batteries. [28]. Moreover, recent developments in reactor design may change this outlook even more, since a recent study suggests [16] that indirectly heated biomass gasification can produce a carbon-rich biochar (>92 %) with increased porosity (89–198 $cm^3$ (STP)/g) and high heating value (28–31 MJ/kg a.r.) from a-quality secondary forest wood pellets. This is achieved by converting wood pellets into syngas in a novel Indirectly Heated Bubbling Fluidized Bed Steam Reformer (IHBFBSR) design [16]. The IHBFBSR gasifier has been built and commissioned by the Dutch company Petrogas - Gas Systems in collaboration with the Process & Energy Department of the Delft University of Technology [29]. The reactor is made of 310S (AISI) steel and stands at a height of approximately 3 m [29].

In this study, we report the electrochemical performance of biographite produced from gasification biochar obtained from an atmospheric pressure 50 kWth IHBFBSR located at the Delft University of Technology followed by a graphitization process. The biochar used for this work has a high carbon content (96 wt%) and low ash content (<5 wt%) [16]. Therefore, this biochar has the potential to produce high quality biographite, reduce pre-treatment steps (e.g., ash or heavy metal removal) and ease the intensity of the graphitization process. Obtaining such highly graphitic carbon is key for providing adequate renewable alternatives for battery anode active material.

In order to determine how well biographite performs in a lithium-ion battery, tests are carried out to assess its key performance characteristics. The performance was assessed using key performance indicators (KPIs) such as gravimetric capacity, stability and rate capability using electrochemical techniques. We compare the gravimetric capacity of lithiation combined with XRD to determine accessibility and the crystallinity/intersheet distancing respectively. In addition, galvanostatic intermittent titration technique (GITT) estimates the effective diffusivity in biographite during lithium intercalation. The feasibility for using this material is shown, combined with characterization experiments that explain the performance. Furthermore, from this data, it is possible to gain information regarding whether the gasification biochar requires post-treatment actions to avoid undesirable characteristics in the biographite. Examples of post-treatment actions include expanding the graphite sheets enabling higher rates and/or other ions species [30], applying coatings or surface functionalization to tune the solid electrolyte interface (SEI) formation [31], and performing mechanical treatments like milling or sieving to optimize the particle size and shape [32].

## 2. Materials and methods

### 2.1. Material synthesis and characterization

The biochar sieve fraction used in this work (1.2 wt % of the original feedstock) was obtained from experiments with two different types of A-quality residual wood (termed Premium Green and Excellent Red), supplied by the company Labee Group Moerdijk BV, the Netherlands. The tests were performed at the IHBFBSR unit located at Delft University of Technology (TU Delft). The studied biochar was produced at 836 °C, $\lambda = 0.20$, $SB = 0.80$ using corundum as bed material with main diameter 490 μm. The carbon content of this biochar is 96.06 wt% and less than 5 wt% ash. A comprehensive characterisation of this material can be found in del Grosso et al. [16]. The IHBFBSR biochar was mixed with iron nitrate [$Fe(NO_3)_3$] with a weight ratio of pure iron to biochar of 20 wt%. This mixture was graphitized in a horizontal tube furnace with a heating rate of 10 °C/min to 1000 °C for 3h. After the graphitization process, iron was removed from the biographite by washing with 0.1 M hydrochloric acid (HCl) followed by ethanol in an ultrasonic bath. The biographite was subsequently filtered and dried at 105 °C for 24h. An iron catalyst was chosen as it has been reported an effective catalyst for the graphitization of waste at relatively low temperatures [1].

XRD measurements of the biographite were performed with a Bruker D8 Advance diffractometer Bragg-Brentano geometry and Lynxeye position sensitive detector with a radiation source of Cu Kα. The divergence slit is V12, the scatter screen height is 5 mm, and the X-ray machine is operated at 45 kV and 40 mA. The Debye–Scherrer equation was used to determine the crystallite size of the biographite. The surface area of the biochar was estimated using $N_2$ physisorption measured at 77 K with an autosorb iQ equipment. The surface area was determined by applying the Brunauer-Emmett-Teller (BET) method. A multi-point BET was carried out. The samples were degassed ($N_2$; 150 °C; 6 h) before proceeding with BET analysis.

### 2.2. Electrode synthesis and characterization

The biographite powder was vigorously mixed with polyvinylidene fluoride (PVDF) binder (Solef 5130, Solvay), conductive additive (Carbon Super C45, Timcal) in a 90:5:5 %m ratio. Solvent N-Methyl-2-pyrrolidone (NMP,anhydrous 99.5 %, Sigma Aldrich) was added in 1:20 m/m ratio with PVDF and thoroughly mixed for an hour using a top stirrer at 1 kRPM (IKA). The anode was cast on copper foil using a doctor blade with a 200 μm blading thickness. The electrode sheet is dried at 60 °C at < 30 mBarA for at least 24 h to remove residual solvent.

Surface analysis of the electrode material is carried out using X-ray

Photoelectron Spectroscopy (XPS). A K-alpha Thermo Fisher Scientific (USA) spectrometer with a monochromatic Al K-alpha source was used with a spot size of 400 μm. Elemental analysis and high energy spectra of Carbon (C 1s) and Oxygen (O 1s) were obtained. Electrode images and Energy dispersive X-ray spectroscopy (EDS) were obtained with Scanning electron microscopy (SEM) using a JEOL JSM-IT700HR FE-SEM setup. EDS using 15 kV acceleration voltage is used to verify the XPS elemental analysis in depth (penetration depth ~ micrometer). The elemental composition of biomass, biochar and biographite comprises: major (>1 % at.), minor (1–0.1 %at.), and trace (<0.1 % at.) elements.

### 2.3. Electrochemical characterization

Half cell (HC) batteries were manufactured versus Lithium metal coin cells and an in-house made 3-point cell (see the Supplementary Information for the cell design). The electrode was punched using a 12.7 mm diameter coin cell electrode punch. For coin cells, CR2032 coins were assembled with Celgard 2400 separator and 15 mm metal discs as counter electrode. As electrolyte 100 μl 1 M $LiPF_6$ in 3:7 EC:EMC v/v + 2 % VC solution was used. The 3 point cell was made using a KF40 flange stub fitted with a teflon ring and EPDM gasket, sealed using a polymer chain clamp (SI Fig. 8). One stub was fitted with a 15 mm diameter copper cylinder and spring, which contained a 15 mm lithium metal disc. The other stub contained the reference wire feed through, which was insulated with kapton cladding. The reference wire was fixed at the feed by using a ferrule fitting that fixed an O-ring from the outside. The working electrode with a 6 mm centre hole was placed on the stub. A flint of lithium metal was inserted in the centre of the hole on the reference wire, in plane with the electrode. To keep the lithium flint in place during closing, a 6 mm diameter non-conductive padding with wire feedthrough was used. The same electrolyte and celgard separator used in the coin cell assembly are used here as well.

Galvanostatic charge/discharge cycling tests were performed between 0 and 1.5 V vs $Li/Li^+$. The cells were cycled in a MACCOR-4000 multichannel battery cell cycler in a climate controlled room at 18 °C. Theoretical gravimetric capacity of graphite is assumed (372 mAh/g, 2.43 mAh/$cm^2$, 1C = 372 mA/g) [6]. Cells were cycled 16 times at 0.1C to compare with typical graphite intercalation potential curves, then cycled at C/2 in CCCV mode. A slow C/50 cycle was performed to assess the available gravimetric capacity after 168 cycles. The 3 point cell was cycled at C/2 for 100 cycles. Before and after the 100 cycles, two cycles at 0.1C were performed.

Particle diffusivity was investigated by combining galvanostatic intermittent titration (GITT) and electrochemical impedance spectroscopy (EIS) during intercalation and deintercalation in a Parstat MC equipped with a PMC200 potentiostat (Ametek). The GITT pulse interval was 30 min at 0.1C with open circuit intervals of 5 min. EIS is used to assess the internal resistances after extended cycling.

## 3. Results and discussions

### 3.1. IHBFBSR biographite structure and composition

The conversion of biomass into biographite is followed by measuring the materials crystallinity with XRD. Fig. 1 presents the XRD results obtained for the raw biomass, biochar and biographite from the IHBFBSR unit. For raw biomass, there are two wide peaks at 2θ = 17° and 23°, which are credited to cellulose and turbostratic crystalline C, respectively [16]. After gasification, the flattening of the biochar peak at 2θ = 17° and 23°, as well as low intensity peak at 2θ = 43.4°, indicates the conversion of amorphous cellulose to biochar with poor crystallinity. Additionally, following graphitization, the biographite shows a high degree of crystallinity with a characteristic peak at 2θ = 26.5° and 44.6°. A d-spacing of 3.4 Å and a crystalline size of 34.29 nm was obtained using Bragg and Debye–Scherrer equations respectively. The d-spacing and crystalline size are in line with precarbonized Fe-catalyzed

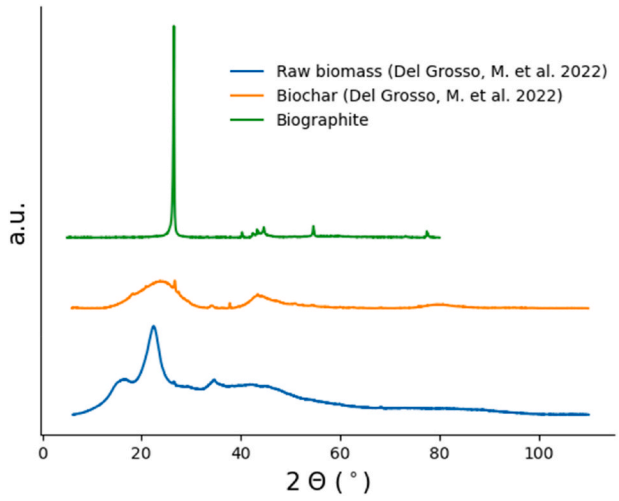


**Fig. 1.** XRD pattern of raw biomass, IHBFBSR biochar and biographite respectively. A sharp peak is observed in the biographite spectrum indicating highly crystalline graphite is obtained after graphitization of IHBFBSR biochar.

graphitized woody materials [1].

The size of crystallites of the gasifier biographite is comparable with results reported for other graphitic carbons produced from pyrolysis of iron-impregnated cellulose (21–31 nm, produced at 1000, 1400, and 1800 °C) [23,33] as well as commercial graphite (47.1 nm) [34]. The advantage of the IHBFBSR biographite over slow pyrolysis is that the biographite exhibits larger crystalline size. The material was also manufactured at a lower temperature of 1000 °C. Furthermore, these data highlight the advantage of using biochar from indirect gasification as a precursor for biographite since high-value syngas is created concurrently, as compared to using slow pyrolysis alone for biographite production. The BET surface area of the biographite is 126.91 $m^2$/g, 58 % lower than the original biochar (300 $m^2$/g [16]). The results indicate that the graphitization process contributed significantly to the closure of the pores, which is consistent with previous research [35]. Nonetheless, the measured surface area is significantly higher than that of Shi et al., [35] (42–93 $m^2$/g) and commercial graphite (5–20 $m^2$/g [36]). Supplementary Information – Table 1 contains detailed data on the nitrogen adsorption isotherm for biographite.

The biographite electrodes have 6.52 ± 0.07 mg/$cm^2$ active material loading and a thickness of 76 μm. The structure of the biographite electrode is shown in Fig. 2 using SEM. The electrode structure shows a homogeneous distribution of particles between 1 and 20 μm (Fig. 2A) on which carbon black (<1 μm) is uniformly deposited. The larger flakes contain traces of Fe (1.6 %m), as indicated from EDS line scan results (SI Fig. 6). Furthermore, the EDS composition (Table 1) indicates minor elements such as Si (0.97 % m), Cl (0.56 % m), Al (0.15 % m) and Ti (0.12 %m). Furthermore, acid washing was successful in eliminating

**Table 1**
Elemental analysis on biographite electrode. EDS is used to obtain elemental composition of micrometer depth. XPS is used to analyze the surface composition.

| Element | EDS Mass% | XPS Mass% |
|---|---|---|
| C | 82.9 | 77.2 |
| O | 6.1 | 6.6 |
| F | 3.3 | 12.8 |
| Fe | 1.6 | NA |
| Cu | 4.3 | 0.1 |
| Si | 1.0 | 1.8 |
| Cl | 0.6 | NA |
| Al | 0.2 | 1 |
| Ti | 0.1 | NA |
| O/C | 7.4 | 8.5 |

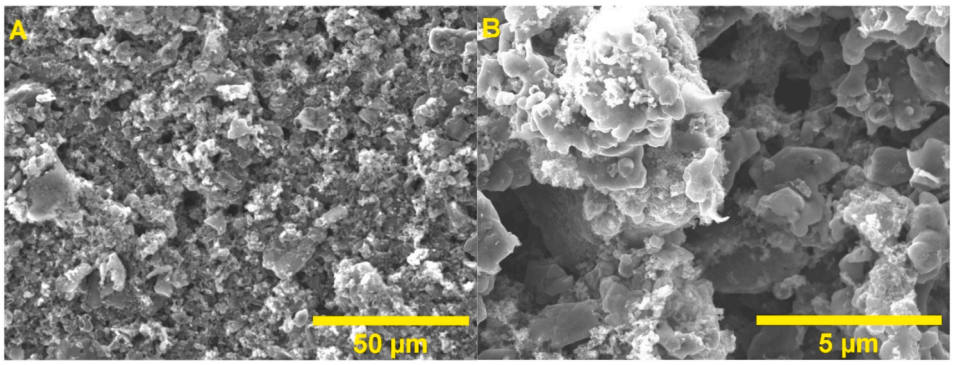


**Fig. 2.** SEM image of Biographite electrode structure. A) A wide particle size distribution is observed on the surface. B) Micrometer sized biographite flakes are covered with (nm sized) carbon black conductive additive particles.

iron impurities, with a surface concentration of 1.6 % (Table 1), which is comparable to other studies that used iron as a catalyst in graphitizing biomass for graphite production [37,38]. To further strip these impurities, it's been shown that increasing the HCl concentration to 2 M during the washing step has been proved to be effective [39]. Si, Al and Ti were already contained in the biochar as reported by Del Grosso et al. [16]. With respect to Cl, this is the result of the acid washing process. There is also a fairly high oxygen amount (6.14 % m) with respect to the carbon (82.86 % m). Also Cu (4.3 % m) is observed, originating from the current collector.

Results from XPS indicate that the biographite near-surface (nm depth) has a high carbon purity level (Table 1). Aside from C, O, F and Si no further elements were detected in the XPS survey spectra. The O/C ratio is higher than EDS (micron depth), indicating that the biographite surface contains oxygenated compounds. Higher magnification SEM image (Fig. 2B) shows that the IHBFBSR biographite exhibits rounder features, which is consistent with biographites derived from iron-catalyzed graphitization of lignocellulosic biomass [40]. Furthermore, the graphite (flakes) and carbon black are well dispersed (Fig. 2B).

### 3.2. IHBFBSR biographite anode performance in lithium batteries

The potential trace of graphite formation versus lithium metal provides valuable information about the presence and extent of side reactivity, as well as graphite exfoliation (Fig. 3B). The potential profile shows an irreversible capacity of 1.67 mAh/cm$^2$, which is 74 % of the

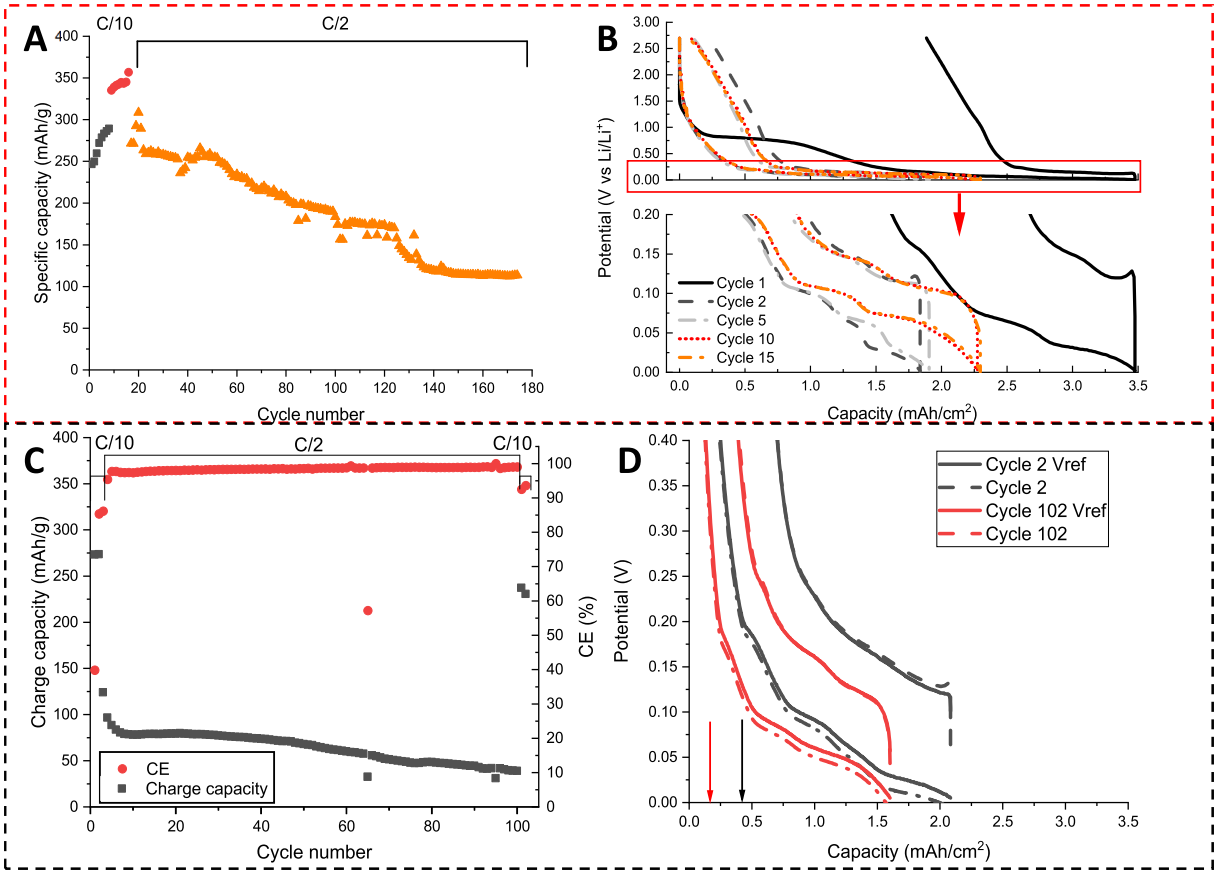


**Fig. 3.** Top: (Dis)charge capacity and coulombic efficiency (A/C) and potential traces (B/D) of biographite:Li HC during long duration cycling (A/B) and in a 3 point electrode cell test (C/D). In the 3 point electrode reference potential Vref shows local potential at the biographite side. Arrows indicate the capacity at which the potential limit was reached during deintercalation.

reversible capacity during discharge, yielding an initial coulombic efficiency (ICE) of 46 % (Fig. 3B, black). This performance is similar to previous studies for biographites from iron-catalyzed graphitization [1]. The majority of the irreversible capacity can be assigned to an additional voltage plateau above 0.8 V versus $Li/Li^+$. The initial irreversible lithiation at such potential can be attributed to the Solid-Electrolyte Interface (SEI) formation by EC decomposition on the graphite active material [31,41]. Compared to typical graphite (76 % ICE) [42], the irreversible capacity is high (46 % ICE) and may be attributed to the (i) high surface area (126.91 $m^2/g$) compared to commercial graphite containing imperfections/impurities (Fig. 2) [12] and (ii) presence of high roughness on the surface which can extend the decomposition of EC-like components. Previous research [35,36,43] indicates that large surface areas may have a negative impact on graphite's electrochemical performance, as there is a nearly linear relationship between irreversible capacity and BET specific surface area.

As can be seen from Fig. 3A, the biographite improves in terms of gravimetric capacity during the first 16 cycles. The intercalation potential and coulombic efficiency after the first two formation cycles improves gradually indicating small losses due to continued side reactivity. At 150 - 100 mV, the graphite lithiation plateau is steep and sloping (Fig. 3B, black), which extends after cycling to the three characteristic intercalation plateaus typical of lithium intercalation in graphite (Fig. 3B, dark grey and grey). Also the overpotential for intercalation lowers (Fig. 3B, cycle 2 dark grey, 1.45 to 1.7 $mAh/cm^2$ and cycle 5 light grey, 1.44 to 2.25 $mAh/cm^2$). One potential explanation is that the graphite interlayer distance grows over time during initial cycling, resulting in increased surface area availability and the development of the second intercalation plateau (Fig. 3B, comparison of potential plateau cycle 2 to 5). At the same time, the overpotential during initial intercalation below 0.75 $mAh/cm^2$ shows negligible change. The electrochemical results support the XRD results showing that the IHBFBSR biographite is highly graphitic, which accounts for its high gravimetric capacity (357 mAh/g, where commercial graphites are nearing 360 mAh/g, e.g. MSE natural graphite). To determine if the material performance improvement is due to electrochemical activity, a short rest period was introduced in the deintercalated state. After four weeks, the initial gravimetric capacity during cycling was enhanced by 16 % (from 289 mAh/g to 335 mAh/g) in cycle 10 (Fig. 3B red), after which further capacity improvement shows a maximum of 357 mAh/g in cycle 16 (Fig. 3A). Improved wetting and/or further expansion of the graphite may provide such improvement during the rest period, leading to nearly full utilization of the graphitic carbon in the 16th cycle. It is worth noting that following the short rest, the overpotential decreases -it costs less energy to lithiate the graphite- but the third plateaus is barely observable (Fig. 3B, red compared to grey).

A prolonged rest period lasting 6 months was implemented following cycle 16 to assess electrode stability (Fig. 3B, orange). After this period, the half cell initially shows a decreased capacity during intercalation at C/10 (293 mAh/g), followed by hysteresis and a significant decline in gravimetric capacity during C/2 cycling, relative to the cycle preceding the prolonged rest period. The specific capacity of 357 mAh/g could not be recovered after prolonged shelf life. From cycle 16 onward, the buildup of internal resistances cause a steep potential decrease during the CC step and current fade during the CV step. A high overpotential during deintercalation is observed as well (SI Fig. 3). A gradual capacity fade is measured till 100 mAh/g in the 160th cycle (Fig. 3A). The half cell testing suffers from continued side reactions on the lithium metal counter electrode side, as shown by EIS (SI Fig. 4). The EIS spectrum shows that the bulk conductivity is decreasing, which has a significant impact on rate performance. Thus, an extended intercalation/deintercalation cycle at 0.02C was performed after prolonged cycling to examine the (de)intercalation performance of the biographite itself. The result shows that the biographite still has a capacity of 265 mAh/g after 168 cycles, which is 98 % of the capacity during the initial cycle and 73 % of the maximum capacity the graphite anode showed before the long rest period. The reversible gravimetric specific capacity is thus retained towards the 169th cycle, which shows 265 mAh/g capacity remains available. The highest observed capacity is however near the theoretical capacity of graphite intercalation (372 mAh/g), showing excellent promise of this material. The characteristic voltage plateaus around 150 mV and 100 mV show high ordering of the graphene layers, characteristic of thermally treated carbons [6].

To rule out the possibility of SEI buildup at the counter electrode as the source of capacity fade, a repeated test was conducted using a three-point cell with a lithium metal reference near the graphite electrode (shown in SI Fig. 8). The three-point cell was cycled at a (dis)charge rate of 0.5C (Fig. 3C). Results indicate that during graphite intercalation, the potential difference between the lithium counter electrode and the reference lithium amounts to 11 mV. The formation was halted to observe the OCP after formation period at cutoff potential of 0.6 V. The open cell potential of 1.2 V indicated negligible intercalation (SI Fig. 7). In SI Fig. 7, between 0.6 and 0.2 V additional side reactivity can be observed which is linked to exfolation of the graphite [44]. During the second cycle, a capacity of 274 mAh/g was detected, after which immediately C/2 cycling was started. Without the rest period an improvement in gravimetric capacity was not observed. After 100 cycles, the cell shows 237 mAh/g capacity, 87 % of the original capacity, which is higher compared to the duration tests but lower compared to commercial analogs (e.g. Yan et al. [45] reporting 98 % after 40 cycles with a similar electrolyte and commercial graphite, which would extrapolate to 95 % after 100 cycles). The exfoliation of graphite flakes, which results in active material contact loss over time, may thus be the dominant capacity fading mechanism during extended cycling.

To facilitate high charge rates, graphite should be highly ordered to allow lithium to diffuse between the sheets. The predicted diffusion coefficients during graphite deintercalation are shown by GITT observations (SI Fig. 5) , which match the general trend of diffusion coefficient progression in commercial graphite materials. [46]. The wide particle size distribution becomes apparent during intercalation. Here, a higher apparent diffusion coefficient is observed. Smaller particles with a larger surface-to-molar volume ratio may operate as a capacitor, temporarily holding a higher fraction of lithium and redistributing it during the rest phase of the GITT process. The heterogeneous particle distribution and presence of impurities in the biographite would cause additional wear on smaller particles during fast charging and charging at lower temperatures [47]. As such, particle heterogeneity should be resolved in a subsequent upgrading step.

There are three characteristics of the IHBFBSR biographite which need improvement to meet with the high lithium-ion battery anode standard. First, the initial coulombic efficiency is too low to directly use graphitized biochar as anode material. Some initial capacity is typically necessary to form a stable SEI [48]. The low ICE found for biographite would result in a loss of lithium inventory in full cell batteries, making the total gravimetric battery capacity low. There are several pretreatment steps to mitigate a low ICE caused by the high amount of surface defects. One approach is to reduce the oxygen content and roughness of the pristine material by chemical treatment or coating [12,49,50]. To sustain the CE during subsequent cycles, the use of electrolyte additives to form a completely stable SEI layer is already well known in literature [20]. Second, as seen in GITT, there is an issue with excessive wear on a fraction of the biographite. The unequal intercalation rates caused by particle heterogeneity are the root cause of this deterioration. In this case, a method involving sieving and milling could be useful. A final concern is the capacity gain and subsequent fade observed after prolonged cycling, which may be attributed to expanding and possibly exfoliation of the biographite. Here, increasing performances may be achieved by forming a robust surface layer with electrolyte additives and/or applying a protective coating, as seen with biographites formed from pyrolysis.

To make an estimate of the potential use of gasification biographites during future studies, the experiments can be shortened to obtain the

key performance parameters using only ICE (SEI formation, potential lithium inventory loss), GITT (particle heterogeneity and rate performance) and a <20 day cycling test at C/2 combined with a 'formation – rest – cycle method' to assess wear, capacity fade mechanisms like contact loss, wetting and/or exfoliation. Due to the large diversity of potential substrates and processing parameters, it is essential to shorten such preliminary studies. With this testing approach it takes less time to investigate the feasibility of using the biographite and the result of subsequent processing strategies for valorization.

## 4. Conclusion

Biographite derived from biochar from indirect biomass gasification (IHBFBSR) yields flake shaped graphite with high carbon to oxygen ratio (93:7).

The highly graphitic nature of the IHBFBSR biographite, evidenced by XRD shows a high reversible capacity useful for LIB, showing almost full gravimetric utility (96 %).

The cycling stability of IHBFBSR biographite directly used as anode in lithium half cells show excellent potential for application in LIB.

By using the biochar fraction produced by biomass gasifiers for battery applications, a greater level of biomass valorization is achieved than that achieved with biographites obtained from pyrolysis.

## CRediT authorship contribution statement

**Mark Weijers:** Writing – original draft, Visualization, Validation, Methodology, Investigation, Formal analysis, Conceptualization. **Fokko M. Mulder:** Writing – review & editing, Supervision, Resources. **Luis Cutz:** Writing – review & editing, Writing – original draft, Conceptualization.

## Data availability

Data is made available on 4TU repository under DOI: www.doi.org/10.4121/a886b7df-d656-4620-8334-c834686e7ab5.

## Acknowledgements

Authors would like to thank Joost Middelkoop for working out the technical drawings of the 3 point electrode design. The authors would also like to thank Hans Brouwer for performing the graphitization experiments.

## Appendix A. Supplementary data

Supplementary data to this article can be found online at https://doi.org/10.1016/j.biombioe.2025.108147.

## Data availability

Data will be made available on request.

## References

[1] T. Vook, et al., Sustainable Li-ion anode material from Fe-catalyzed graphitization of paper waste, J. Energy Storage 73 (2023) 109242.
[2] S. Ragan, H. Marsh, Science and technology of graphite manufacture, J. Mater. Sci. 18 (1983) 3161–3176.
[3] European Commission, Directorate General for Internal Market, Industry, Entrepreneurship and SMEs. *Study on the Critical Raw Materials for the EU 2023: Final Report*, Publications Office, LU, 2023.
[4] A. Gomez-Martin, et al., Iron-catalyzed graphitic carbon materials from biomass resources as anodes for lithium-ion batteries, ChemSusChem 11 (2018) 2776–2787.
[5] N.A. Banek, D.T. Abele, K.R. McKenzie Jr., M.J. Wagner, Sustainable conversion of lignocellulose to high-purity, highly crystalline flake potato graphite, ACS Sustainable Chem. Eng. 6 (2018) 13199–13207.
[6] Advanced Batteries, Springer US, Boston, MA, 2009, https://doi.org/10.1007/978-0-387-76424-5.
[7] Z. Shi, et al., Establishment of green graphite industry: graphite from biomass and its various applications, J. Power Sources. Adv. 3 (2023) 402–415.
[8] P. Li, H. Kim, S.-T. Myung, Y.-K. Sun, Diverting exploration of silicon anode into practical way: a review focused on silicon-graphite composite for lithium ion batteries, Energy Storage Mater. 35 (2021) 550–576.
[9] D.H.S. Tan, et al., Carbon-free high-loading silicon anodes enabled by sulfide solid electrolytes, Science 373 (2021) 1494–1499.
[10] C. Fang, X. Wang, Y.S. Meng, Key issues hindering a practical lithium-metal anode, Trends Chem. 1 (2019) 152–158.
[11] G.M. Hobold, et al., Moving beyond 99.9% coulombic efficiency for lithium anodes in liquid electrolytes, Nat. Energy 6 (2021) 951–960.
[12] Y.P. Wu, C. Jiang, C. Wan, R. Holze, Effects of pretreatment of natural graphite by oxidative solutions on its electrochemical performance as anode material, Electrochim. Acta 48 (2003) 867–874.
[13] D.L. Wood, J. Li, C. Daniel, Prospects for reducing the processing cost of lithium ion batteries, Journal of Power Sources 275 (2015) 234–242.
[14] M. Greenwood, M. Wentker, J. Leker, A bottom-up performance and cost assessment of lithium-ion battery pouch cells utilizing nickel-rich cathode active materials and silicon-graphite composite anodes, Journal of Power Sources Advances 9 (2021) 100055.
[15] J. Shankar Tumuluru, S. Sokhansanj, J.R. Hess, C.T. Wright, R.D. Boardman, REVIEW: a review on biomass torrefaction process and product properties for energy applications, Ind. Biotechnol. 7 (2011) 384–401.
[16] M. Del Grosso, et al., Influence of indirectly heated steam-blown gasification process conditions on biochar physico-chemical properties, Fuel Process. Technol. 235 (2022) 107347.
[17] Y. Li, et al., Hydrothermally assisted conversion of switchgrass into hard carbon as anode materials for sodium-ion batteries, ACS Appl. Mater. Interfaces 16 (2024) 28461–28472.
[18] L. Cutz, H. Maldonado, G. Zambrano, M. Al-Naji, W. de Jong, Hydrothermal liquefaction of elaeis guineensis trunks: lessons learned from a case study in Guatemala, Ind. Crop. Prod. 206 (2023) 117552.
[19] L. Cutz, N. Bias, M. Al-Naji, W. de Jong, Exploring the catalytic hydrothermal liquefaction of Namibian encroacher bush, Sci. Rep. 15 (2025) 112.
[20] A. Eldesoky, et al., Impact of graphite materials on the lifetime of NMC811/Graphite pouch cells: part II. long-term cycling, stack pressure growth, isothermal microcalorimetry, and lifetime projection, J. Electrochem. Soc. 169 (2022) 010501.
[21] S.C. Yi, et al., Effects of fir-wood biochar on CH4 oxidation rates and methanotrophs in landfill cover soils packed at three different proctor compaction levels, Sci. Total Environ. 907 (2024) 167951.
[22] W.-J. Liu, H. Jiang, H.-Q. Yu, Emerging applications of biochar-based materials for energy storage and conversion, Energy Environ. Sci. 12 (2019) 1751–1779.
[23] W.J. Sagues, et al., A simple method for producing bio-based anode materials for lithium-ion batteries, Green Chem. 22 (2020) 7093–7108.
[24] Y.W. Yap, et al., Recent advances in synthesis of graphite from agricultural bio-waste material: a review, Materials 16 (2023) 3601.
[25] G. Enaime, A. Baçaoui, A. Yaacoubi, M. Lübken, Biochar for wastewater treatment—conversion technologies and applications, Appl. Sci. 10 (2020) 3492.
[26] EBC, European Biochar Certificate - Guidelines for a Sustainable Production of Biochar, 2022.
[27] L. Fryda, R. Visser, Biochar for soil improvement: evaluation of biochar from gasification and slow pyrolysis, Agriculture. 5 (2015) 1076–1115.
[28] L. Lower, et al., Catalytic graphitization of biocarbon for lithium-ion anodes: a minireview, ChemSusChem 16 (2023) e202300729.
[29] C. Tsekos, M. del Grosso, W. de Jong, Gasification of woody biomass in a novel indirectly heated bubbling fluidized bed steam reformer, Fuel Process. Technol. 224 (2021) 107003.
[30] H. Buqa, D. Goers, M. Holzapfel, M.E. Spahr, P. Novák, High rate capability of graphite negative electrodes for lithium-ion batteries, J. Electrochem. Soc. 152 (2005) A474.
[31] Ph Bernardo, et al., Influence of graphite surface properties on the first electrochemical lithium intercalation, Carbon 49 (2011) 4867–4876.
[32] F. Röder, S. Sonntag, D. Schröder, U. Krewer, Simulating the impact of particle size distribution on the performance of graphite electrodes in lithium-ion batteries, Energ. Tech. 4 (2016) 1588–1597.
[33] A.C. Ghogia, L.M. Romero Millán, C.E. White, A. Nzihou, Synthesis and growth of green graphene from biochar revealed by magnetic properties of iron catalyst, ChemSusChem 16 (2023) e202201864.
[34] M.A. Lopez quintela, Method for Obtaining Graphene Sheets, 2014.
[35] Z. Shi, et al., Bio-based anode material production for lithium–ion batteries through catalytic graphitization of biochar: the deployment of hybrid catalysts, Sci. Rep. 14 (2024) 3966.
[36] M. Winter, P. Novák, A. Monnier, Graphites for lithium-ion cells: the correlation of the first-cycle charge loss with the brunauer-emmett-teller surface area, J. Electrochem. Soc. 145 (1998) 428.
[37] L. Gai, J. Li, Q. Wang, R. Tian, K. Li, Evolution of biomass to porous graphite carbon by catalytic graphitization, J. Environ. Chem. Eng. 9 (2021) 106678.
[38] E. Thompson, A.E. Danks, L. Bourgeois, Z. Schnepp, Iron-catalyzed graphitization of biomass, Green Chem. 17 (2015) 551–556.
[39] J. Ren, et al., Low-temperature-pyrolysis preparation of nanostructured graphite towards rapid potassium storage with high initial coulombic efficiency, Nano Res. 17 (2024) 5138–5147.

[40] R.D. Hunter, J. Davies, S.J.A. Hérou, A. Kulak, Z. Schnepp, Milling as a route to porous graphitic carbons from biomass, Philos. Trans. A Math. Phys. Eng. Sci. 379 (2021) 20200336.
[41] P. Novák, et al., The complex electrochemistry of graphite electrodes in lithium-ion batteries, Journal of Power Sources 97–98 (2001) 39–46.
[42] X. Li, et al., Review on comprehending and enhancing the initial coulombic efficiency of anode materials in lithium-ion/sodium-ion batteries, Nano Energy 77 (2020) 105143.
[43] T. Placke, et al., Assessment of surface heterogeneity: a route to correlate and quantify the 1st cycle irreversible capacity caused by SEI formation to the various surfaces of graphite anodes for lithium ion cells, Z. Phys. Chem. 229 (2015) 1451–1469.
[44] D. Goers, M.E. Spahr, A. Leone, W. Märkle, P. Novák, The influence of the local current density on the electrochemical exfoliation of graphite in lithium-ion battery negative electrodes, Electrochim. Acta 56 (2011) 3799–3808.
[45] Z. Yan, M.N. Obrovac, Electrolyte reactivity on graphite and copper as measured in lithium double half cells, J. Electrochem. Soc. 164 (2017) A2977–A2986.
[46] J.H. Park, H. Yoon, Y. Cho, C.-Y. Yoo, Investigation of lithium ion diffusion of graphite anode by the galvanostatic intermittent titration technique, Materials 14 (2021) 4683.
[47] M. Kim, I. Kim, J. Kim, J.W. Choi, Lifetime prediction of lithium ion batteries by using the heterogeneity of graphite anodes, ACS Energy Lett. 8 (2023) 2946–2953.
[48] S.J. An, et al., The state of understanding of the lithium-ion-battery graphite solid electrolyte interphase (SEI) and its relationship to formation cycling, Carbon 105 (2016) 52–76.
[49] X. Cui, et al., Pretreatment of graphite anodes with lithium sulfate to improve the cycle performance of lithium-ion batteries, Energy Technol. 5 (2017) 549–556.
[50] M. Gaberscek, Improved carbon anode for lithium batteries pretreatment of carbon particles in a polyelectrolyte solution, Electrochem. Solid State Lett. 3 (1999) 171.